

Origin of spin reorientation and intrinsic anomalous Hall effect in the kagome ferrimagnet TbMn_6Sn_6

D. Connor Jones,^{1,2,*} Suvadip Das,^{1,2,3,*} Hari Bhandari,^{1,2,*} Xiaoxiong Liu,⁴ Peter Siegfried,^{1,2} Madhav P. Ghimire,^{5,6} Stepan S. Tsirkin,^{4,7,8} I. I. Mazin,^{1,2} and Nirmal J. Ghimire^{1,2,9,10,†}

¹*Department of Physics and Astronomy, George Mason University, Fairfax, Virginia 22030, USA*

²*Quantum Science and Engineering Center, George Mason University, Fairfax, Virginia 22030, USA*

³*Department of Physics, Birla Institute of Technology and Science*

Pilani Hyderabad Campus, Hyderabad, Telangana 500078, India

⁴*Department of Physics, University of Zurich, Winterthurerstrasse 190, Zurich CH-8057, Switzerland*

⁵*Central Department of Physics, Tribhuvan University, Kirtipur, Kathmandu 44613, Nepal*

⁶*Leibniz Institute for Solid State and Materials Research,*

IFW Dresden, Helmholtzstr. 20, D01069 Dresden, Germany

⁷*Centro de Física de Materiales, Universidad del País Vasco, 20018 San Sebastián, Spain*

⁸*Ikerbasque Foundation, 48013 Bilbao, Spain*

⁹*Department of Physics and Astronomy, University of Notre Dame, Notre Dame, Indiana 46556, USA*

¹⁰*Stavropoulos Center for Complex Quantum Matter,*

University of Notre Dame, Notre Dame, Indiana 46556, USA

TbMn_6Sn_6 has attracted a lot of recent interest for a variety of reasons, most importantly, because of the hypothesis that it may support quantum-limit Chern topological magnetism, derived from the kagome geometry. Besides, TbMn_6Sn_6 features a highly unusual magnetic reorientation transition about 100 K below the Curie point, whereby all spins in the system, remaining collinear, rotate by 90° . In this work, we address both issues combining experiment, mean-field theory and first-principle calculations. Both magnetic reorientation and the unusual temperature dependence of the anomalous Hall conductivity (AHC) find quantitative explanation in the fact that Mn and Tb, by virtue of the Mermin-Wagner theorem, have very different spin dynamics, with Tb spins experiencing much more rapid fluctuation. We were able to cleanly extract the intrinsic AHC from our experiment, and calculated the same microscopically, with good semiquantitative agreement. We have identified the points in the band structure responsible for the AHC and showed that they are not the kagome-derived Dirac points at the K-corner of the Brillouin zone, as conjectured previously.

INTRODUCTION

The kagome lattice, a two-dimensional network composed of corner-sharing triangles, can harbor complex magnetic and electronic properties, including frustrated, non-collinear and non-coplanar spins [1–4], interesting electronic features, such as flat bands and Dirac points (DP), quantum spin liquids, and integer and fractional quantum Hall states [5–10].

Recently there has been growing interest in the three-dimensional (3D) compounds consisting of kagome nets of magnetic atoms. Their symmetry-protected Dirac crossings can, by virtue of the exchange splitting, become Weyl points, and after inclusion of spin-orbit coupling may give rise to interesting topological properties [5–10]. RMn_6Sn_6 ($R166$), where R is a rare-earth element, are a recent addition to this class of compounds [11–17]. There, the Mn atoms form the kagome net in the basal plane of the hexagonal crystal structure as shown in Fig. 1(a,b). The $R166$ compounds are rich in magnetic phases unlike other kagome magnets, due to their unique crystal structure [13, 18–21], making these compounds an excellent platform to investigate the in-

terplay of magnetism and the electronic structure.

While the well-known 2D Kagome cuprates [22, 23] (herbertsmithite *etc.*) have been attracting a lot of interest due to their in-plane magnetic frustration and proximity to spin liquids, 3D stannates are dramatically different in their physical properties. Those cuprates are both electronically and magnetically extremely 2D. Their magnetic interactions are dominated by the frustrated antiferromagnetic (AF) in-plane Heisenberg exchange, while the electronic structure is well mappable onto a single-orbital nearest-neighbor tight binding model [5]. On the contrary, the stannates are good metals where the in-plane interactions are driven by kinetic exchange and therefore strongly ferromagnetic (FM) (no in-plane frustration), and their electronic structure is multiorbital and very 3D like. As a result, their interplanar magnetic interactions are long-ranged and of variable sign, and their electronic structure is complex and dispersive in all three directions, with only mild reminiscences of the notorious Dirac cones and flat bands, characteristic of the single-orbital 2D Kagome model (the latter are known to be particularly fragile and rather far from true “flatness” even in herbertsmithite-type compounds [5]). This makes the physics and topology of stannates, and especially this 166 family, much more complex than that of this “zero” model, but also much more interesting.

* equal contribution

† corresponding author; nghimire@nd.edu

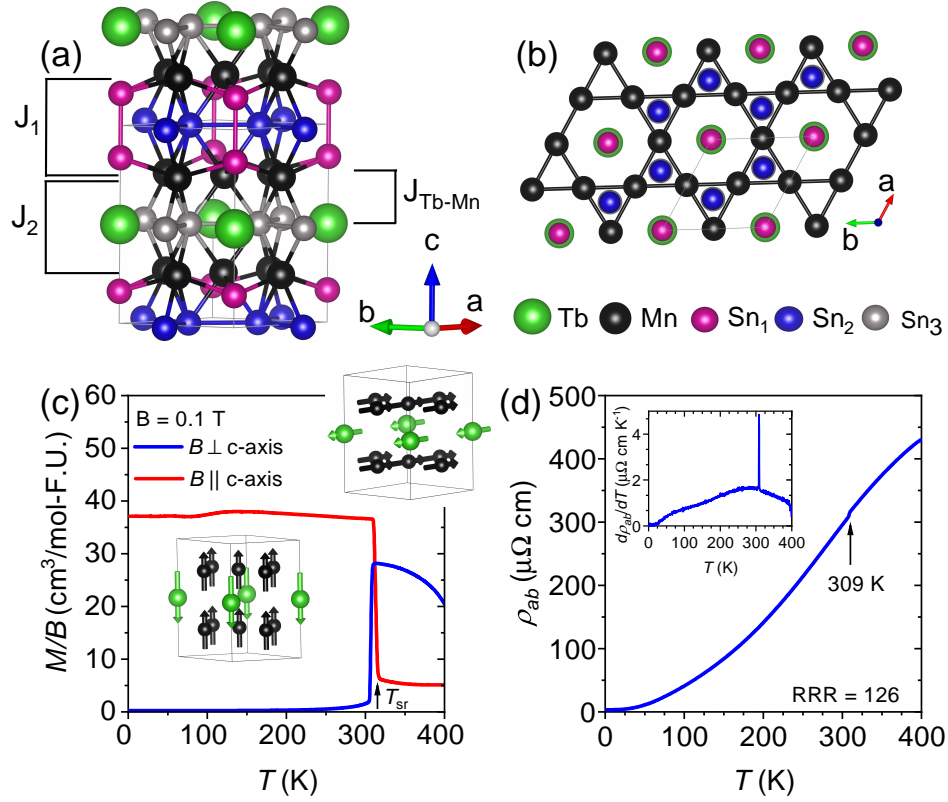


FIG. 1 : Crystal structure and characterization of TbMn_6Sn_6 . (a) Sketch of crystal structure of TbMn_6Sn_6 . The symbols J_i are exchange constants between different Mn layers. $J_{\text{Tb-Mn}}$ is the exchange constant between Tb and Mn layers. (b) Top view of the structure shown in (a) within a unit cell shown by the grey solid lines where there are two kagome planes of Mn atoms with the formula Mn_3Sn separated by Sn_3 and TbSn_2 layers. (c). Field-cooled (FC) magnetic susceptibility of TbMn_6Sn_6 as a function of temperature measured parallel (red curve) and perpendicular (blue curve) to the crystallographic c -axis. At $T_{sr} = 309$ K, the susceptibilities abruptly change directions indicating reorientation of the spins as illustrated by the two cubic graphics in the inset. The orientation of the Tb (green) and Mn (black) magnetic moments above and below T_{sr} from right to left, respectively. (d) Electrical resistivity of TbMn_6Sn_6 as a function of temperature. Inset shows the temperature derivative of the resistivity revealing the spin-reorientation transition at 309 K in the resistivity measurement.

Their magnetic phase diagrams are extremely rich, and, with an exception of YMn_6Sn_6 (Y166), poorly understood. Some of them show unconventional Hall behavior [13, 24], including fluctuation-driven topological Hall effect (in Y166) [13] and large anomalous Hall conductivity [11, 12, 15, 17].

TbMn_6Sn_6 (Tb166) orders in a collinear in-plane ferrimagnetic (FiM) spin structure below 423 K [18, 25]. Highly unusual, with the decrease in temperature, at $T_{sr} = 309$ K it experiences a sudden spin reorientation, where the moments spontaneously rotate from the basal plane toward the c -axis, and quickly set entirely along c , as can be seen in the magnetic susceptibility anisotropy, and illustrated by the sketch of the spin structure in Fig. 1(c). All Mn spins are parallel to each other and antiparallel to the Tb spins. Tb is tri-valent, *i.e.*, isovalent with Y, and has 8 f -electrons with the total magnetic moment of $9 \mu_B$ (6 from the spins and 3 from the orbital moments). Additionally, Tb166 is a good metal with a

large residual resistivity ratio (RRR), which is 126 in our sample as shown in Fig. 1(d).

Recently, tunneling experiments [12] revealed a surface band of Tb166 with a gapped DP (“Chern gap”) at about 130 meV above the Fermi energy (E_F), which in a pure 2D case would have provided for an anomalous Hall conductivity (AHC) comparable with the experiment. Based on their band structure calculations, Ref. [12] suggested that it was located at the K point in the Brillouin zone. However, the calculated bands presented there had an implicit offset of the Fermi energy (E_F) by about 0.5 eV (see a detailed discussion in Ref. [26]), which can hardly be the case in the bulk. On the other hand, anomalous Hall effect is a bulk property that comes from the Berry curvature of all the occupied states see Eq. 2 in the Methods Section). Its estimation requires full calculations of the Berry curvature, taking into account *all* electronic states, and not only those in the vicinity of one particular point in the Brillouin zone

(BZ). It thus calls for a detail analysis of the band structure and calculations of the contributions of these bands to the AHC. Also, a detailed understanding of the role of the element Tb in establishing the collinear FiM order and spin reorientation transition is essential. A comparison of both magnetic and magnetotransport properties with the sister compound Y166 is extremely helpful.

In this paper, we investigate these three issues by combining experimental observations and first principles calculations. First, we show that different dynamics of spin fluctuations on Tb and on Mn plays a key role in the spin reorientation process. We then show that although Tb166 exhibits a large intrinsic AHC, the separation of its intrinsic and extrinsic contributions is quite complex and in this scenario, spin dynamics is crucially important and should be taken into account in analyzing the AHC in R166 compounds. Our calculations reveal that the AHC in Tb166 results from a combination of multiple factors and states across different regions of the 3D BZ, rather than from one particular point in the BZ. We find that contrary to the “zero model”, the near-Fermi level DP in Tb166, while can still be, with some imagination, identified at the K-H line in the BZ, are highly dispersive; the band that generates the largest contribution to the AHC in our calculations is derived from Mn d_{z^2-1} orbitals and is located around 1 eV above the Fermi level at K point and around 1 eV below it at H point. The two DPs closest to the Fermi level at the K-point (see Ref. [26] for a comprehensive discussion of high-symmetry DPs), at ≈ -50 and $\approx +230$ meV, contribute basically nothing, nor does the DP identified in [12], which is situated at $\approx +700$ meV in the bulk. A significant contribution to the AHC comes from where the Dirac lines cross the Fermi level (one for spin up and the other for spin-down), which occurs at $k_z \approx 0.25$ r.l.u. (reciprocal lattice units). Additionally, there are several accidental (some of them tilted) DPs near the Fermi level, which also contribute to the Berry curvature and Hall conductivity. Amongst them, the most notable is the spin-down Dirac line crossing the Fermi level at the midpoint between A and L ($k_z=0.5$ r.l.u.), with some contribution from an accidental tilted spin-up DP between K and Γ .

METHODS

Single crystals of TbMn₆Sn₆ were grown by a self-flux method using excess Sn as the flux. Tb pieces (Alfa Aesar 99.9 %), Mn pieces (Alfa Aesar 99.95 %), and Sn shots (Alfa Aesar 99.999 %) were loaded to a 2 mL aluminum oxide crucible in a molar ratio of 1:6:20 and sealed in a fused silica ampule under vacuum. The sealed ampule with the crucible was heated to 1150 °C for 10 hours, homogenized at 1150 °C for 12 hours, and then cooled to 650 °C at 4 °C/hour. Once the furnace reached 650 °C, the excess Sn-flux was decanted using a centrifuge. Many well faceted hexagonal single crystals

were obtained in the crucible. The crystal structure was verified using powder x-ray diffraction at room temperature using a Rigaku MiniFlex diffractometer. A small amount of the crystals from each batch were ground into powder. These powder samples were used to collect x-ray diffraction patterns, (shown in Supplementary Fig. S1) for one representative batch, using Rietveld refinement [27] with the FULLPROF software [28]. The results of the refinement are presented in Supplementary Table S1. Magnetic and transport measurements were performed on single crystals oriented for c -axis.

DC magnetization, resistivity, and Hall measurements were performed in a Quantum Design Dynacool Physical Property Measurement System (PPMS) with a 9 T magnet. The AC Measurement System (ACMS) option was used for the DC magnetization measurements. The saturation magnetization and coercive fields were calculated by averaging between the heights and widths of the hysteresis curves, respectively, from the magnetization data with the magnetic field B parallel to c axis. The resistivity and Hall measurements employed the conventional four-probe method by attaching 25 μ m diameter platinum wires with Epotek H20E silver epoxy. 2 mA of electrical current was used for the transport measurements. The contact misalignment, in magnetoresistance and Hall measurements, was corrected by field symmetrization and antisymmetrization of the measured data, respectively.

The first principles calculations for electronic and magnetic structure of Tb166 were performed utilizing the local density approximation with the Perdew-Burke-Ernzerhof (PBE) gradient correction, (GGA) for the exchange-correlation functional, orthogonal plane-wave basis sets and the pseudopotential method to account for electron-ion interactions as implemented in the integrated suite for electronic structure calculation Quantum Espresso [29]. The Tb pseudopotential in our calculations include the 4f electrons within the open-core model. Note that inclusion of the 4f electrons in the valence configuration, with a sizeable Hubbard interaction U for f electrons, does not alter the low energy electronic structure significantly. The single-particle wave functions were evaluated using a plane-wave energy cutoff of 600 Ry. We utilized the Wannier90 [30] program to generate maximally localized Wannier functions (MLWFs) from the Bloch states by convolution with unitary matrices and minimizing the spread of the MLWFs in real space. The method is independent of the choice of basis sets for the Bloch functions and the locality of MLWFs could be exploited to derive accurate band structures and low energy Fermi surface properties at considerably less computational cost. Note that we have included the effect of spin-orbit coupling in our first-principles calculations during the evaluation of the anomalous Hall conductivity at the level of constructing the maximally localized Wannier functions. Adopting the Kubo formalism, the intrinsic contribution to the anomalous Hall

conductivity can be written as: [31, 32]

$$\sigma_{\alpha\beta}^{AHE} = \frac{e^2}{\hbar} \sum_{n \neq n'} \int \frac{d^3\mathbf{k}}{(2\pi)^3} [f(\varepsilon_n(\mathbf{k})) - f(\varepsilon_{n'}(\mathbf{k}))] \times \text{Im} \frac{\langle n, \mathbf{k} | v_\alpha(\mathbf{k}) | n', \mathbf{k} \rangle \langle n', \mathbf{k} | v_\beta(\mathbf{k}) | n, \mathbf{k} \rangle}{[\varepsilon_n(\mathbf{k}) - \varepsilon_{n'}(\mathbf{k})]^2} \quad (1)$$

where f_{nk} are the Fermi Dirac distribution functions. Equivalently, Eq. 1 can be rewritten as: [33–35]

$$\begin{aligned} \sigma_{\sigma\beta}^{AHE} &= -\frac{e^2}{\hbar} \epsilon_{\alpha\beta\gamma} \int \frac{d^3\mathbf{k}}{(2\pi)^3} \Omega_\gamma(\mathbf{k}) \\ &= -\frac{e^2}{\hbar} \sum_n \epsilon_{\alpha\beta\gamma} \int \frac{d^3\mathbf{k}}{(2\pi)^3} f_{n,\mathbf{k}} \Omega_\gamma(n, \mathbf{k}) \end{aligned} \quad (2)$$

Here, the anomalous Berry term is obtained by convolution of the Berry curvature with that of the Fermi function and summed over all the occupied states, where the Berry curvature can be written in terms of the Bloch functions as

$$\Omega_\gamma(n, \mathbf{k}) = i \langle \nabla_{\mathbf{k}} u_n(\mathbf{k}) | \times | \nabla_{\mathbf{k}} u_n(\mathbf{k}) \rangle \quad (3)$$

While several electronic structure codes [30, 36] exist for evaluation of Berry curvature in real materials, we used the WannierBerri code [37] in order to reach high precision in the evaluation of AHC. Namely, our procedure incorporates minimal-distance replica selection method [38] for accurate Wannier interpolation and the recursive adaptive refinement for accurate determination of physical quantities by the integration of rapidly oscillating functions in the \mathbf{k} -space for evaluation of the anomalous Hall coefficient and appropriate consideration of symmetry properties. Selected calculations were verified against the full potential local-orbital (FPLO) code [39], where the linear tetrahedron method was employed with $12 \times 12 \times 6$ \mathbf{k} mesh.

RESULTS AND DISCUSSION

Magnetism

We first discuss the ferrimagnetic (with all Mn spins parallel) rather than pseudo-antiferromagnetic state in Y166, and then the easy-axis magnetic anisotropy of Tb166 developed below the spin reorientation temperature ($T_{sr} = 309$ K). We begin with the much better understood spiral ground state of Y166. It was appreciated decades ago that this spiral can be exceedingly well described in a three-parameters mean-field 1D Heisenberg chain model, where the Mn planes are ferromagnetically ordered, the interplanar exchange *via* the Sn_3 layer, J_1 is ferromagnetic, the one *via* the YSn_2 layer, J_2 , is antiferromagnetic, and the second-neighbors interplanar exchange, J_3 , is ferromagnetic [19] [Fig. 1(a)].

We have demonstrated recently that this model, augmented with single-site anisotropy and anisotropic exchange, fully described the complex magnetic phase diagram in this compound [13].

When Y is substituted with a magnetic ion, such as Tb, its magnetic interaction with the Mn plane must be taken into account. Regardless of its sign, this interaction can be integrated out yielding an effective ferromagnetic interaction $\tilde{J}_2 = -2J_{\text{Mn-Tb}}$ (here and below we absorb the SS' factor into the definition of J). This interaction is rather strong and overwhelms the direct antiferromagnetic J_2 one. Given that $|J_3| \ll |J_2|, |J_1|$, the resulting magnetic Hamiltonian is not frustrated, and the system readily orders ferrimagnetically (the actual sign of $J_{\text{Mn-Tb}}$ is antiferromagnetic [26]). This is also fully consistent with our first principles calculations.

Next, we look at the magnetic anisotropy. It is instructive to compare the behavior of the 166 compounds across the entire series of rare earths. At the onset of magnetic ordering, all of them have easy plane anisotropy [18]. [Except for the spiral-magnetic R166 ($R = \text{Sc}, \text{Y}, \text{Lu}$) and Tm166, they all form collinear ferrimagnetic structures]. The non-magnetic rare earths (Y, Lu and Sc) retain this easy plane anisotropy all the way down to low temperatures, and so does Gd, which has a full f-shell and no single-ion magnetic anisotropy. This clearly establishes the fact that Mn anisotropy (both single site and exchange) in 166 compounds is easy plane. Er and Tm present an interesting case: they form antiferromagnetic (Er) or short-pitch spiral (Tm) structures, indicating that the transferred interaction \tilde{J}_2 in these materials is weaker than J_2 , so the net interaction is still antiferromagnetic. As a result, Mn– R interaction is frustrated (and $R - R$ one very weak), so the R sublattice remains disordered till rather low temperatures (75 and 58 K, respectively), and even after ordering does not couple with the Mn sub-lattice, and thus does not affect its anisotropy.

The most interesting situation emerges in Tb, Dy, Ho and Er. There, \tilde{J}_2 is strong enough to induce a collinear state. Given the hexagonal crystal field, the natural lowest-order magnetic anisotropy for these R ions is uniaxial, and strong. Detailed calculations [26] show that in all the cases the net anisotropy *at zero temperature* is dominated by the R , and dictates the magnetization direction for the entire crystal. The crystal field on the R site being comparable with, or smaller than the SOC, the total energy is determined by the transformation of the corresponding spherical harmonics between the spin tilting angle and the crystallographic z axis, which for f-ions include terms of up to M_z^6 with comparable coefficients. Direct calculations [26] have demonstrated that, indeed, the magnetic anisotropy energies for (Tb–Er)166 include quartic, and likely sextic terms, which generate low-symmetry zero-temperature anisotropy in Ho166 and Dy166.

Let us now quantify this physical picture in reference to, specifically, Tb166, and address the reorienta-

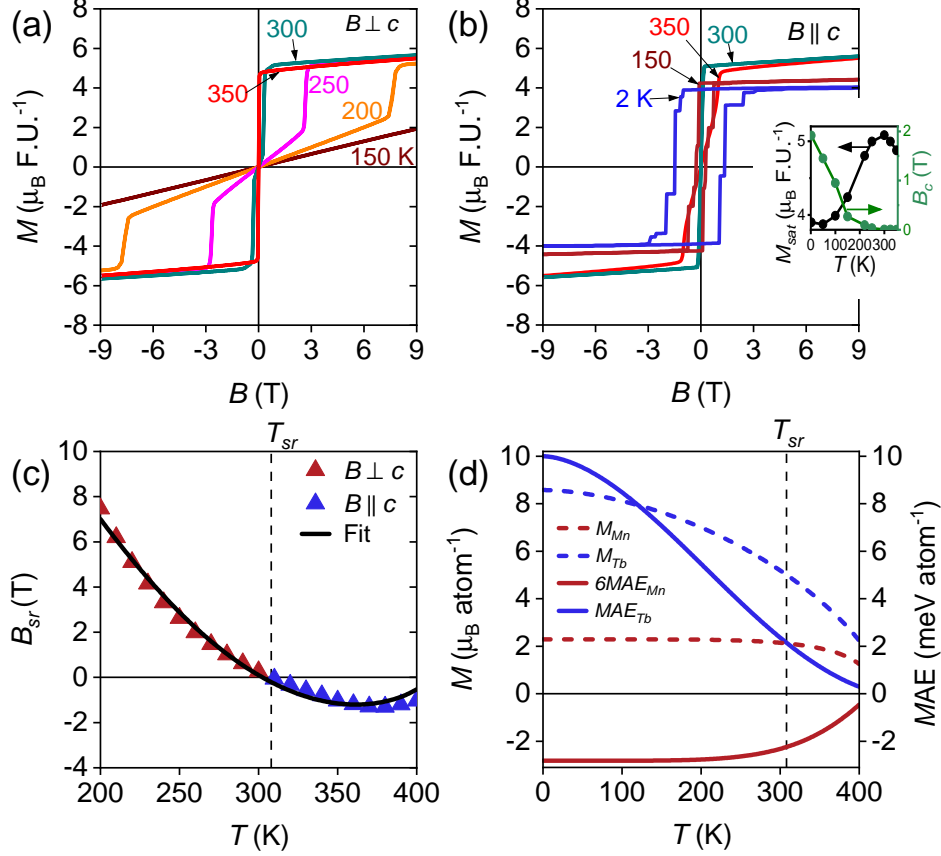


FIG. 2 : Magnetic field dependence of magnetization with a) $B \perp c$ and b) $B \parallel c$. The inset in panel (b) shows the temperature dependence of saturation magnetization and the critical field. (c) Magnetic phase diagram for the spin-reorientation transition. Positive values for B corresponds to $B \perp c$ whereas negative values correspond to $B \parallel c$. The fitted curve with $K_{Mn} = -8.96 \times 10^{-2} \text{ meV} \mu_B^{-2}$ and $K_{Tb} = 0.136 \text{ meV} \mu_B^{-2}$ is observed on top of the experimental values. The dashed vertical line represents the zero-field spin reorientation transition temperature T_{sr} . (d) Temperature dependence of the magnetic moments on Mn (red) and Tb (blue) (dashed lines) from Ref. [25], and magnetic anisotropy energies (\mathcal{MAE}) of the Mn (red) and Tb (blue) sublattices (solid lines) [$\mathcal{MAE}_{Mn}(0) = -0.47 \text{ meV Mn}^{-1}$ and $\mathcal{MAE}_{Tb}(0) = 10 \text{ meV Tb}^{-1}$].

tion transition at higher temperature. First, let us show our experimental data. The external field dependence of magnetization $M(B)$ with $B \perp c$ and $B \parallel c$ is shown in Figs. 2(a) and 2(b), respectively. For $B \perp c$, the shape of the curves indicates a soft ferromagnetic behavior above T_{sr} via a sharp increase at low fields followed by saturation at higher fields. Below T_{sr} , a metamagnetic transition is observed that corresponds to the spins flopping from the c -axis to the basal plane. The metamagnetic transition field increases with the decrease in temperature and surpasses 9 T below 150 K. For $B \parallel c$, the curves also display soft ferromagnetic behavior above 250 K. Even above T_{sr} , the spins are flopped from the basal plane with relatively smaller magnetic field. Below 250 K a hard ferromagnetic behavior is observed via the emergence of hysteresis loops containing asymmetric steps, which increase in width with decreasing temperature attaining a coercive field of 2 T at 2 K [inset of Fig. 2(b)]. The saturation magnetization M_{sat} reaches

approximately $3.9 \mu_B \text{ F.U.}^{-1}$ at 2 K and increases up until around 300 K [inset of Fig. 2(b)]. The metamagnetic transition for $T < T_{sr}$ with $B \perp c$ [Fig. 2(a)] and $T > T_{sr}$ with $B \parallel c$ [Fig. 2(b)] (tracked by dM/dB in Fig. S2) represents the critical field required to induce a spin-reorientation transition $B_{sr}(T)$ at a particular temperature. A critical field -temperature phase diagram is shown in Fig. 2(c). At higher temperatures, the magnetocrystalline anisotropy along the kagome planes dominates, resulting in the “easy-plane” type ordering, similar to Y166 in the ground state. Below T_{sr} the uniaxial anisotropy of the Tb-sublattice dominates. In addition to this zero field spin-reorientation, at any temperature, the spin-reorientation transition in Tb166 can also be induced by applying an external field B_{sr} along the hard magnetization direction, that takes place through a first order magnetization process (FOMP).

Now let us rationalize and quantify these observations. The effective Heisenberg Hamiltonian for the \tilde{J}_2

exchange reads:

$$H_2 = -2|J_{Mn-Tb}|\cos(\theta/2), \quad (4)$$

while the effective magnetic anisotropy Hamiltonian (absorbing, as usual, the anisotropic exchange into the single site anisotropy) is (see Supplementary Note 1 for details)

$$E_{anis} = 6\mathcal{MAE}_{Mn}(T) + \mathcal{MAE}_{Tb}(T), \quad (5)$$

with

$$\mathcal{MAE}_i(T) = K_i M_i^2(T) \frac{M_i^2(0)}{3M_i^2(0) - 3M_i(0)M_i(T) + M_i^2(T)},$$

where \mathcal{MAE} is the T -dependent magnetic anisotropy energy, M_i and K_i are the ordered (*i.e.*, averaged over thermal fluctuations) magnetic moments and 2^{nd} order anisotropy coefficients for the two atoms and sublattices ($i = \text{Mn, Tb}$), respectively. In the mean-field approximation $M_{Mn}(T)$ and $M_{Tb}(T)$ [Fig. 2(d)], can be described by the Brillouin functions. Importantly, the molecular (Weiss) mean field on the Mn sites is large and is equal to $6J_{in-plane} \sim 3000 \text{ K} \gg T_C$, while that on the Tb site is much smaller, $6J_{Mn-Tb} \sim 600 \text{ K}$ [26], comparable with T_C . As a result, the ordered magnetic moment on the Tb site shown by blue dashed line in Fig. 2(d), as probed by neutrons, exhibit a much more gradual temperature decline (essentially mean field), while that on the Mn site (red dashed line) changes slowly (according to its larger Curie-Weiss temperature, T_{CW}), until it rapidly drops near T_C , which is strongly reduced from T_{CW} by 2D (Mermin-Wagner) fluctuations.

This is illustrated in Fig. 3, showing fluctuating moments at $T \ll T_C$ and $T \lesssim T_C$. Correspondingly, the relative contribution of Tb into the overall anisotropy energy gets smaller as the temperature is increased and leads to the reorientation transition, above which the total anisotropy is dominated by Mn. Note that in this model, neglecting higher order anisotropy term, the transition is first order; this is not true in Dy166 and Ho166, where the higher order terms lead to an incomplete reorientation.

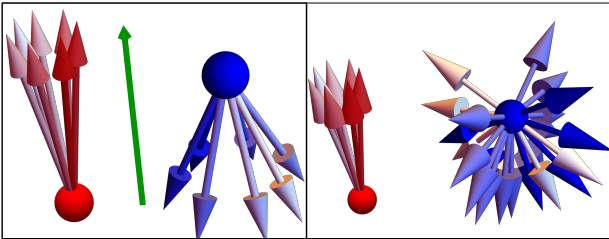


FIG. 3 : Cartoon illustrating the spin dynamics of Mn (red) and Tb (blue) spins at low (left) and high (right) temperatures. The green arrow shows the net magnetization direction.

Fig. 2(d) uses Curie-Weiss parameters fitted to existing neutron powder diffraction data [25]. As Fig. S3 shows, the fitting is very good. By equating E_{anis} [Eq. (2)] to the single-site Zeeman energy at $B = B_{sr}$, given by

$$E_{Zeeman}(T, B_{sr}) = [M_{Tb}(T) - 6M_{Mn}(T)]\mu_B\mu_0 B_{sr}(T),$$

where μ_B is the Bohr magneton, a fitted curve for $\mu_0 B_{sr}(T)$ is generated in Fig. 2(c) with $K_{Mn} = -8.96 \times 10^{-2} \text{ meV}\mu_B^{-2}$ and $K_{Tb} = 0.136 \text{ meV}\mu_B^{-2}$. The negative sign of K_{Mn} indicates that the Mn sublattice favors the easy-plane magnetization direction. Conversely, the positive sign of K_{Tb} indicates that the Tb sublattice favors the easy-magnetization direction along the c -axis due to a hexagonal crystal field splitting, as discussed above. Moreover, because Tb^{3+} is a heavier ion, the magnitude of K_{Tb} is significantly larger than K_{Mn} , thereby contributing more to E_{anis} for a given M_i [26]. Therefore, the remarkable agreement of the fitted curve [Fig. 2(c)] with the experimental data reveals that the spin-reorientation phase diagram is quantitatively described by the temperature dependencies of M_{Mn} and M_{Tb} . The calculated values for $\mathcal{MAE}_{Mn}(T)$ and $\mathcal{MAE}_{Tb}(T)$ are shown in Fig. 2(d) by red and blue solid lines, respectively. Analogous to M_{Mn} and M_{Tb} , respectively, \mathcal{MAE}_{Mn} remains relatively constant from around 300 K down to zero temperature whereas \mathcal{MAE}_{Tb} dramatically increases with decreasing temperature. At T_{sr} , $\mathcal{MAE}_{Mn} \sim -\mathcal{MAE}_{Tb}$, revealing that the spin reorientation transition at zero-field occurs when the two competing anisotropy energies of the two sublattice FiM system cancel out. In the ground state, $\mathcal{MAE}_{Mn} = -0.47 \text{ meV}$ per Mn and $\mathcal{MAE}_{Tb} = 10.0 \text{ meV}$ per Tb. To understand the contributions of Heisenberg exchange and single-site anisotropy terms within \mathcal{MAE}_{Mn} , we compare with the YMn_6Sn_6 compound. A recent study by Ghimire et al. [13] estimated \mathcal{MAE}_{Mn} for YMn_6Sn_6 in ground state to be $\sim -0.12 \text{ meV}$ per Mn atom. By assuming the single-site anisotropy on Mn- and Tb-sub-lattices coexist independently, we argue the larger magnitude of \mathcal{MAE}_{Mn} for Tb166 arises from J_{Mn-Tb} exchange. Recently, Lee et al. [26] calculated magnetic anisotropy of Tb166 excluding Tb f -electrons to be $-1.7/2 = -0.85 \text{ meV}$. This large value can be assigned to the anisotropy of the d electrons on Tb, included in Ref. [26] together with that of Mn. Please note that in Fig. 2(c) we only show spin-reorientation fields above $T \approx 200 \text{ K}$. The reason is that the formalism presented above models single-site magnetic anisotropies as quadratic functions of the fluctuation-average moments. This is a good approximation for Mn d -electrons, but for Tb it is known [26] to include large quartic and even sextic terms; this makes the quadratic approximation increasingly less reliable at low temperatures, where the average magnetic moment on Tb is large.

Anomalous Hall effect

Now we discuss the anomalous Hall effect (AHE), which has attracted considerable attention recently in the RMn_6Sn_6 compounds [11–15, 17]. An AHE is the transverse voltage induced by a longitudinal current flow in ferromagnetic materials without an external magnetic field. The AHE can have both intrinsic and extrinsic contributions. The former comes from the Berry curvature of the electronic bands, whereas the latter is related to the electron scattering effects such as side jumps and skew scattering. One of the biggest challenges in studying AHE is separating the intrinsic AHE from the extrinsic ones. In an ideal crystal at zero temperature the latter is zero, and so is the longitudinal resistivity ρ_{xx} which led to the idea of using a protocol that relates σ_{xy}^A to ρ_{xx} via a power expansion,

$$\rho_{yx}^A = a + b\rho_{xx} + c\rho_{xx}^2 + d\rho_{xx}^3 + \dots \quad (6)$$

$$\sigma_{xy}^A = a\sigma_{xx}^2 + b\sigma_{xx} + c + d/\sigma_{xx} + \dots, \quad (7)$$

with the idea that the free term c in Eq. 7 (or the coefficient of the quadratic term in Eq. 6) will represent the intrinsic AHC (the terms higher than quadratic are neglected). It was rather soon realized, however, that the extrinsic AHC scales differently with ρ_{xx} of different origin. The widely discussed ones are skew scattering and side jumps. The contribution from the former is proportional to the resistivity, while that from the latter is proportional to the square of the resistivity, thus complicating the extraction of the intrinsic AHE. Furthermore, if there are several mechanisms for residual resistivity (impurities, defects, domain walls) the coefficients may be different for different mechanism (see a detailed discussion of this issue in Ref. [40]). In ferromagnetic materials scaling of the AHC can be influenced by phonon and magnon contributions that can vary significantly with temperature. While Ref. [41] argued convincingly that phonon scattering does not contribute to the linear term in Eq. 6 (and equivalently in Eq. 7) because of the sign-changing potential fluctuations that phonons generate, it is not clear whether the same argument can be applied to transverse magnons, which represent fluctuations around a given average magnetic direction. To the best of our knowledge, a theory of AHE in presence of fluctuating localized spins has never been developed.

Not surprisingly, given all these pitfalls and caveat, in real life the simplified version of Eqs. 6 and 7 that is ubiquitously used is: [12, 42, 43],

$$\rho_{yx}^A(T) = a + c\rho_{xx}^2(T), \quad (8)$$

$$\text{or, } \sigma_{xy}^A(T) = a\sigma_{xx}^2 + c, \quad (9)$$

Even a more sophisticated version presented in Ref. [40] where ρ_{yx}^A takes the form:

$$\begin{aligned} \rho_{yx}^A(T) = & \alpha_I \rho_{xx}^I \rho_{xx}(T) + \beta_I \rho_{xx}^I \\ & + \alpha_P \rho_{xx}^P \rho_{xx}(T) + \beta_P \rho_{xx}^P + \gamma \rho_{xx}^2(T), \end{aligned} \quad (10)$$

where everything but $\rho_{xx}(T)$ is a temperature-independent parameter characterizing different scattering mechanism ($\alpha_{I,P}$ are side-jump coefficients due to impurity/phonon scatterings, and $\beta_{I,P}$ are the skew-scattering coefficient due to impurity, and phonon-impurity cross scattering), often fails to describe the experimental data.

We measured the Hall resistivity of Tb166 as a function of magnetic field $[\rho_{yx}(B)]$ between 1.8 and 300 K as shown by some representative data in Figure 4(a). The zero field value of ρ_{yx} gives the anomalous Hall resistivity ρ_{yx}^A . At higher temperatures, $\rho_{yx}(B)$ follows the magnetization $M(B)$ and shows saturation behavior when the latter saturates, indicating that magnons play a decisive role in high-temperature transport. Below 60 K, although $M(B)$ shows a pronounced hysteresis, the hysteresis in $\rho_{yx}(B)$ becomes unresolvable within the error of the Hall resistivity measurement and makes it difficult to extract ρ_{yx}^A unambiguously (see Fig. S4). In Fig. 4(b) we show the anomalous Hall conductivity $\sigma_{xy}^A = \rho_{yx}^A / \rho_{xx}^2$ (which holds for $\rho_{yx} \ll \rho_{xx}$ as is the case in TbMn₆Sn₆) and longitudinal conductivity $\sigma_{xx} = 1/\rho_{xx}$ as a function of temperature. We can see clearly that σ_{xy}^A shows temperature dependence in the entire temperature range, complicating the extraction of the temperature independent intrinsic Hall conductivity. Not surprisingly, Fig. 4(c) shows that σ_{xy}^A is not linear in σ_{xx}^2 , as expected in Eq. 9 [the black solid line in Fig. S5(a) is plotted using the parameters a' , and c' obtained from a straight line fit to ρ_{yx}^A vs ρ_{xx}^2]. Here, we want to point out that our ρ_{yx}^A vs. ρ_{xx}^2 is similar to that reported in Ref. [12] where Eq. 8 (equivalent of Eq. 9) is used to extract the intrinsic AHC (see Fig. S5). The poor quality of Eq. 8 fit, when plotted in the proper scale, was also noticed in Ref. [44], who used instead Eq. 7 with a non-zero b ; this led to a considerably improved, but still far from perfect fit.

On the other hand, a closer look at the data in Fig. 4(c) shows that σ_{xy}^A can be extremely well described by the relation:

$$\sigma_{xy}^A = a\sigma_{xx}^2 + d/\sigma_{xx} + c \quad (11)$$

as shown by the red curve in Fig. 4(c). Comparing this with Eq. 9 we observe that the main difference with the conventional expression is that the inverse term in σ_{xx} (equivalently, the cubic term in Eq. 6) cannot be neglected. We do *not* observe this term to be significant in the sister compound Y166 [45], which strongly suggests that it is due to scattering off of Tb magnons, in agreement with the arguments above.

The T -dependent term in $\sigma_{xy}^A(T)$ is due to impurity/defect scattering (cf. Eq. 10); indeed, above 150 K, the data can also be fitted just to $\sigma_{xy}^A = c + d/\sigma_{xx}$ [green curve in Fig. 4(c)] yielding about the same value for $c = \sigma_{int}^A$, indicating that the inverse term in σ_{xx} at higher temperatures is essential. The value of σ_{int}^A obtained from the fitting is $140 \pm 1 \text{ S cm}^{-1}$. Although extrinsic effects, primarily, side jumps can also contribute

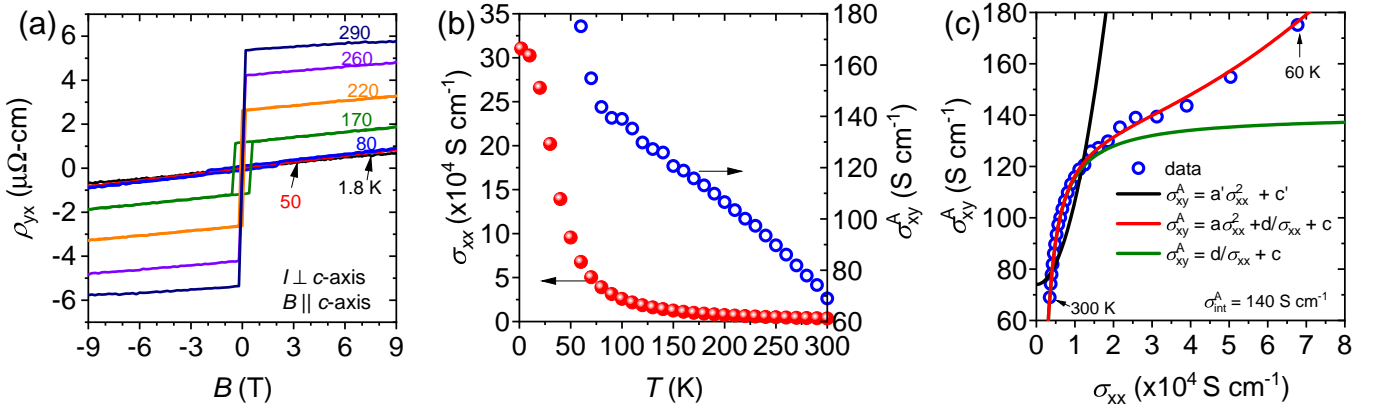


FIG. 4 : a) Anomalous Hall resistivity (ρ_{yx}) of TbMn₆Sn₆ as a function of magnetic field (B) at some representative temperatures. b) Longitudinal conductivity (σ_{xx} , red spheres), and anomalous Hall conductivity (σ_{xy}^A , blue circles) as a function of temperature. c) σ_{xy}^A (blue circles) as a function of σ_{xx} between 300 K (bottom left) and 60 K (top right). The solid lines are the plot of different functions shown in the legend. a , c and d 's are constants. σ_{int}^A is the temperature independent intrinsic anomalous Hall conductivity given by the temperature independent term c . The solid black line uses the parameters a' , c' obtained from the linear fit of the ρ_{yx}^A vs ρ_{xx}^2 , for data presented in Fig. S5(a).

to σ_{int}^A , which complicates comparison with theoretical models, it is likely subdominant [46] and hence it is clear that TbMn₆Sn₆ has a significant intrinsic AHC. What makes Tb166 unique is the presence of the σ_{xx}^{-1} term, indicating an unconventional transport scattering most likely coming from Tb magnons. We emphasize that the same physics that controls the spin-reorientation transition also defines this unusual AHC scaling.

Next, we focus on the evaluation of intrinsic σ_{int}^A and study it microscopically utilizing Density Functional Theory (DFT) and maximally localized Wannier functions (MLWF), as described in the Methods section. Fig. 5(a-f) shows the Wannier-interpolated electronic structure for TbMn₆Sn₆. We note that five Mn d orbitals in the two spin directions per each of the two Kagome layers provide a multitude of Dirac lines along the K-H, reminiscent of the single-orbital 2D tight-binding model. Many propitious features are washed out by interorbital hybridization, but at least 8 are reasonably well expressed. Of them, two spin-up DP are located at -50 and $+200$ meV below (above) the Fermi level. In addition, there are a number of DPs not related to this TB model; for instance, two spin-up DPs occur at M, at -50 and -200 meV, plus, there are about a dozen of accidental DPs all over the BZ, only a few of them relevant for AHC.

Two further DPs are noticeable: one is formed by the spin-down d_{z^2-1} (a_{1g} , in hexagonal notations) Mn orbital; at K it occurs at ~ 0.7 eV above E_F , and extremely rapidly disperses down, crossing the Fermi level midway between K and H. The other one is derived from the $x^2 - y^2 \pm ixy$ orbital and is truly 2D. This is the orbital that was postulated in Ref. [12] to be responsible for the large AHC. However, as was convincingly demonstrated in Ref. [26], in a charge-balanced sys-

tem this band is located about 0.7 eV above the Fermi level, and cannot contribute to AHC. This conclusion fully agrees with our independent calculations, as well as with recently published calculations from the Weizmann group [44]. It is worth noting that this state, being very 2D, is unlikely to dominate the STM spectra, which are normally sensitive to states extending into the vacuum, and k_z -dispersive.

In order to gain microscopic insight into the origin of the large AHC, we performed first principles calculations of the latter, using the code and methodology described in Ref. [33, 34]. Our calculations have been extensively tested for convergence and precision with respect to k -mesh size and higher energy cutoffs. The calculated AHC [37] as a function of the position of the Fermi level is shown in Fig. 6. At the theoretical E_F , it is $50 \pm 1 \text{ S cm}^{-1}$, in qualitative agreement with the experiment, but underestimating the latter by some 60%. For the Fermi level shifted up by ~ 50 meV, corresponding to the about 0.5 $e/\text{formula}$ doping (note that we suggest that our samples are actually doped, it just illustrates the sensitivity of the final result to this parameter), the calculated σ_{xy} is $\sim 80 \text{ S cm}^{-1}$, reducing the discrepancy to $\sim 40\%$. The remaining disagreement, apart from purely technical reasons, may be due to an additional extrinsic contribution, or, even more likely, to underestimation of the correlation effects on Mn. For instance, it was shown that in Sr₂RuO₄ the effective spin-orbit coupling in dynamical mean field calculations is enhanced by a factor of two compared to DFT [47]. It is worth noting that the AHC calculations are known to be extremely sensitive to the details of the computational setup, much more so than the band structure itself. In this regard, recent calculations of AHC [44], while finding overall a rather similar structure of AHC,

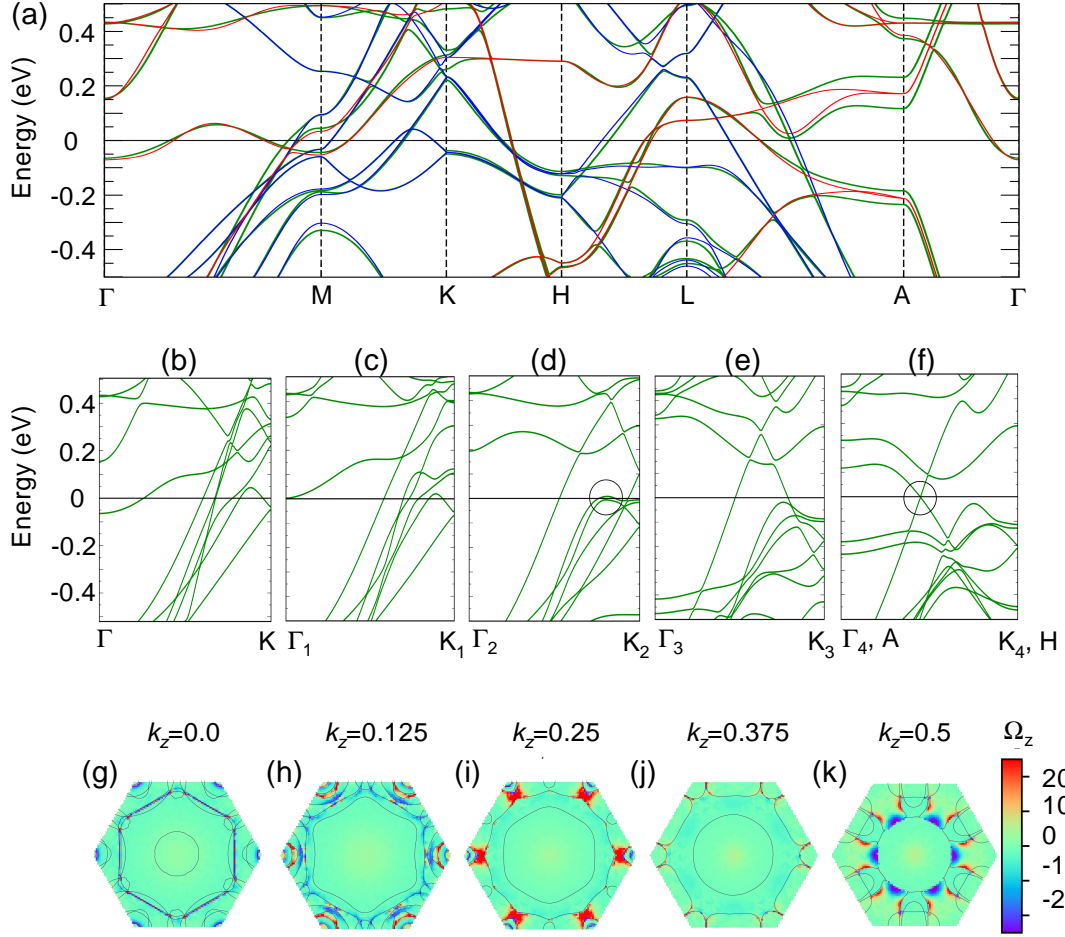


FIG. 5 : The calculated band structure and band/momentum-resolved Berry curvature. (a) Spin-up (blue), spin-down (red) and spin-orbit (green) bands. (b-f) Bands along the generalized Γ -K directions; Γ_i - K_i correspond to $k_z = 0.125, 0.25$, and 0.375 r.l.u for $i = 1 - 3$. No-subscript points refer to actual Γ -K ($k_z = 0$), and $i = 4$ to the AH direction ($k_z = 0.5$). (g-k) Berry curvature Ω_z at different points in the BZ. Panels from left to right correspond to the same k_z and panels in (b-f). The largest positive contribution comes from $k_z \approx 0.25$, negative from $k_z \approx 0.5$; the corresponding parts of the band structure are encircled in (d), and (f), respectively.

differ in some fine details near the Fermi energy. Having discussed this discrepancy with the authors of Ref. [44], we have come together to the conclusion that this difference is due to slightly different computational setups. While this discrepancy does not affect our qualitative conclusion, it also serves as an independent test of the accuracy of the first principles calculations of AHC.

Valuable information can be derived from the color maps showing the contribution to the Berry curvature (essentially, to AHC) from different points in the BZ [Figs. 5(g-k)]. Interestingly, the K-point, conjectured in Ref. [12] to be the sole source of the AHC in Tb166, contributes very little, while large contributions come from two other regions: one arises from complicated hybridization between the DP at K_2 , emanating from the lowest-energy unoccupied DP at K, an avoided acciden-

tal tilted Dirac crossing between K_2 and Γ_2 (spin-up), and an accidental spin-down DP between A and L.

CONCLUSIONS

We have presented combined experimental and theoretical studies of magnetic properties of TbMn₆Sn₆ in comparison to its f-electron-less analogue YMn₆Sn₆ in order to clarify the following issues:

1. Why is TbMn₆Sn₆ a collinear ferrimagnet while YMn₆Sn₆ is a spiral antiferromagnet?
2. Why does TbMn₆Sn₆ experience a spontaneous magnetic reorientation transition ≈ 100 K below its Curie temperature?

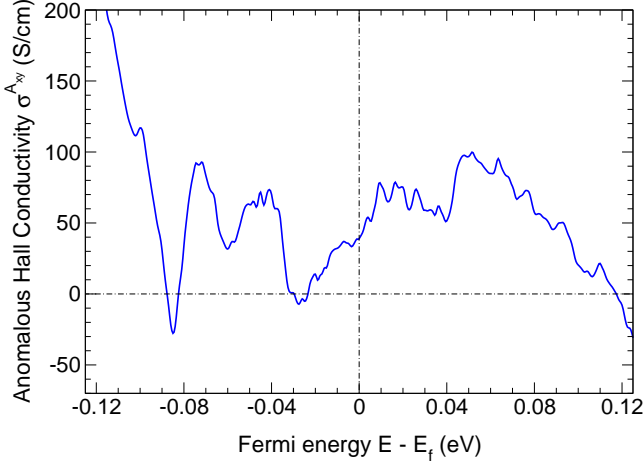


FIG. 6 : The anomalous Hall conductivity σ_{xy}^A as a function of $E - E_F$, obtained by applying iterative adaptive refinement, as described in the recent implementation for extraction of berry curvature.

3. What is the microscopic origin of the anomalous Hall effect in TbMn_6Sn_6 ?
4. What are the scaling relations between the Hall conductivity and longitudinal resistivity in this compound?

After a careful analysis of the experimental and computational data, we have arrived at the following conclusions:

1. Indirect exchange between the two Mn layers bridged by Tb, after integrating out Tb moments, leads to an effective ferromagnetic coupling, rendering an unfrustrated magnetic Hamiltonian. This is in contrast to the Y based analogues as well as other non-magnetic rare earths-based ones.
2. The spin orientation is decided by the competition between the easy-axis Tb anisotropy and the easy plane Mn anisotropy. For fully ordered magnetic moments the former is much larger; however, the Tb and Mn spins have very different thermal dynamics. The molecular (Weiss) field on the Mn site is much larger due to the very strong ferromagnetic in-plane Mn-Mn exchange, while the molecular field on Tb is much weaker. As a result, with the increase in temperature, Tb spins fluctuate more strongly as compared to those of Mn. Due to

the fluctuations, Tb moment gets considerably reduced on approaching the Curie temperature (T_C); so does its magnetic anisotropy, which at ~ 100 K below T_C drops below the Mn anisotropy. This scenario is qualitatively consistent with published neutron scattering and DFT results.

3. The 3D nature of the Fermi surface is important in understanding the anomalous Hall effect in Tb166 . The AHC is not related to a single K-point Dirac cone associated with the single band 2D tight-binding Kagome model, but rather comes from other bands.
4. Magnon contribution, in addition to the impurity scattering and the temperature independent intrinsic AHC, may be important in the scaling relation between the AHC and the longitudinal conductivity in Tb166 .

ACKNOWLEDGMENTS

The authors thank Predrag Nikolic, Patrick Bruno, Jairo Sinova, and especially Liqin Ke, and Binghai Yan, the authors of, respectively, Refs. [26, 44], for insightful discussions. Crystal growth and characterization work at George Mason University is supported by the U.S. Department of Energy, Office of Science, Basic Energy Sciences, Materials Science and Engineering Division. H.B. acknowledges support from the NSF CAREER award DMR-2343536. I.I.M. acknowledges support from the U.S. Department of Energy through the Grant No. DE-SC0021089, and, at a later stage, from National Science Foundation through the Grant No. DMR-2403804. M.P.G. thanks the University Grants Commission, Nepal for the Collaborative Research Grants (Award No. CRG-78/79 S&T-03), and acknowledges the Alexander von Humboldt Foundation, Germany for the equipment grants. M.P.G. thanks Manuel Richter for the fruitful discussions and Ulrike Nitzsche for the technical assistance. S.S.T. acknowledges funding by MCIN/AEI/10.13039/501100011033 through Grant No. PID2021-129035NB-I00, by European Union (Grants No. H2020-MSCA-COFUND-2020-101034228- WOLFRAM2, No. ERCStG-Neupert757867-PARATOP), and by Grant No. PP00P2-176877 from the Swiss National Science Foundation. X.L. acknowledges support from the China Scholarship Council (CSC).

REFERENCES

-
- [1] L. Balents, Spin liquids in frustrated magnets., *Nature* **464**, 199 (2010).
 - [2] H. Chen, Q. Niu, and A. H. MacDonald, Anomalous Hall Effect Arising from Noncollinear Antiferromagnetism,

- Phys. Rev. Lett.* **112**, 017205 (2014).
- [3] S. Sachdev, Kagomé - and triangular-lattice heisenberg antiferromagnets: Ordering from quantum fluctuations and quantum-disordered ground states with unconfined bosonic spinons, *Phys. Rev. B* **45**, 12377 (1992).
 - [4] M. Hirschberger, T. Nakajima, S. Gao, L. Peng, A. Kikkawa, T. Kurumaji, M. Kriener, Y. Yamasaki, H. Sagayama, H. Nakao, K. Ohishi, K. Kakurai, Y. Taguchi, X. Yu, T. hisa Arima, and Y. Tokura, Skyrmion phase and competing magnetic orders on a breathing kagomé lattice, *Nature Communications* **10**, 5831 (2019).
 - [5] I. I. Mazin, H. O. Jeschke, F. Lechermann, H. Lee, M. Fink, R. Thomale, and R. Valentí, Theoretical prediction of a strongly correlated Dirac metal, *Nature Communications* **5**, 4261 (2014).
 - [6] A. Bolens and N. Nagaosa, Topological states on the breathing kagome lattice, *Physical Review B* **99**, 165141 (2019).
 - [7] H. M. Guo and M. Franz, Topological insulator on the kagome lattice, *Physical Review B* **80**, 113102 (2009).
 - [8] Z.-Y. Zhang, The quantum anomalous Hall effect in kagomé lattices., *J. Phys.: Condens. Matter* **23**, 365801 (2011).
 - [9] G. Xu, B. Lian, and S. C. Zhang, Intrinsic Quantum Anomalous Hall Effect in the Kagome Lattice $\text{Cs}_2\text{LiMn}_3\text{F}_{12}$, *Phys. Rev. Lett.* **115**, 1 (2015).
 - [10] E. Tang, J. W. Mei, and X. G. Wen, High-temperature fractional quantum hall states, *Phys. Rev. Lett.* **106**, 236802 (2011).
 - [11] T. Asaba, S. M. Thomas, M. Curtis, J. D. Thompson, E. D. Bauer, and F. Ronning, Anomalous Hall effect in the kagome ferrimagnet GdMn_6Sn_6 , *Phys. Rev. B* **101**, 174415 (2020).
 - [12] J.-X. Yin, W. Ma, T. A. Cochran, X. Xu, S. S. Zhang, H.-J. Tien, N. Shumiya, G. Cheng, K. Jiang, B. Lian, Z. Song, G. Chang, I. Belopolski, D. Multer, M. Litskevich, Z.-J. Cheng, X. P. Yang, B. Swidler, H. Zhou, H. Lin, T. Neupert, Z. Wang, N. Yao, T.-R. Chang, S. Jia, and M. Zahid Hasan, Quantum-limit Chern topological magnetism in TbMn_6Sn_6 , *Nature* **583**, 533 (2020).
 - [13] N. J. Ghimire, R. L. Dally, L. Poudel, D. C. Jones, D. Michel, N. T. Magar, M. Bleuel, M. A. McGuire, J. S. Jiang, J. F. Mitchell, J. W. Lynn, and I. I. Mazin, Competing magnetic phases and fluctuation-driven scalar spin chirality in the kagome metal YMn_6Sn_6 , *Sci. Adv.* **6**, eabe2680 (2020).
 - [14] W. Ma, X. Xu, J.-X. Yin, H. Yang, H. Zhou, Z.-J. Cheng, Y. Huang, Z. Qu, F. Wang, M. Z. Hasan, and S. Jia, Rare Earth Engineering in RMn_6Sn_6 (R = Gd-Tm, Lu) Topological Kagome Magnets, *Phys. Rev. Lett.* **126**, 246602 (2021).
 - [15] G. Dhakal, F. C. Kabeer, A. K. Pathak, F. Kabir, N. Poudel, R. Filippone, J. Casey, A. P. Sakhyia, S. Regmi, C. Sims, K. Dimitri, P. Manfrinetti, K. Gofryk, P. M. Oppeneer, and M. Neupane, Anisotropically large anomalous and topological Hall effect in a kagome magnet, *Phys. Rev. B* **104**, L161115 (2021).
 - [16] G. Venturini, B. Malaman, G. Le Caër, and T. Mazet, Magnetic structures of Mn-rich and of Fe-rich $\text{TmMn}_{6-x}\text{Fe}_x\text{Sn}_6$ stannides with (Mn, Fe) kagome networks and related ^{119}Sn hyperfine magnetic fields, *Phys. Rev. B* **104**, 184433 (2021).
 - [17] H. Zeng, G. Yu, X. Luo, C. Chen, C. Fang, S. Ma, Z. Mo, J. Shen, M. Yuan, and Z. Zhong, Large anomalous Hall effect in kagomé ferrimagnetic HoMn_6Sn_6 single crystal, *Journal of Alloys and Compounds* **899**, 163356 (2022).
 - [18] D. M. Clatterbuck and K. A. G. Jr, Magnetic properties of RMn_6Sn_6 (R = Tb, Ho, Er, Tm, Lu) single crystals, *Journal of Magnetism and Magnetic Materials* **207**, 78 (1999).
 - [19] E. V. Rosenfeld and N. V. Mushnikov, Double-flat-spiral magnetic structures: Theory and application to the RMn_6X_6 compounds, *Physica B* **403**, 1898 (2008).
 - [20] P. E. Siegfried, H. Bhandari, D. C. Jones, M. P. Ghimire, R. L. Dally, L. Poudel, M. Bleuel, J. W. Lynn, I. I. Mazin, and N. J. Ghimire, Magnetization-driven Lifshitz transition and charge-spin coupling in the kagome metal YMn_6Sn_6 , *Communications Physics* **5**, 58 (2022).
 - [21] R. L. Dally, J. W. Lynn, N. J. Ghimire, D. Michel, P. Siegfried, and I. I. Mazin, Chiral properties of the zero-field spiral state and field-induced magnetic phases of the itinerant kagome metal YMn_6Sn_6 , *Phys. Rev. B* **103**, 094413 (2021).
 - [22] V. R. Shaginyan, V. A. Stephanovich, A. Z. Msezane, G. S. Japaridze, J. W. Clark, M. Y. Amusia, and E. V. Kirichenko, Theoretical and experimental developments in quantum spin liquid in geometrically frustrated magnets: a review, *Journal of Materials Science* **55**, 2257 (2020).
 - [23] C. Broholm, R. J. Cava, S. A. Kivelson, D. G. Nocera, M. R. Norman, and T. Senthil, Quantum spin liquids, *Science* **367**, eaay0668 (2020).
 - [24] Q. Wang, K. J. Neubauer, C. Duan, Q. Yin, S. Fujitsu, H. Hosono, F. Ye, R. Zhang, S. Chi, K. Krycka, H. Lei, and P. Dai, Field-induced topological Hall effect and double-fan spin structure with a *c*-axis component in the metallic kagome antiferromagnetic compound YMn_6Sn_6 , *Phys. Rev. B* **103**, 014416 (2021).
 - [25] B. C. E. Idrissi, G. Venturini, and B. Malaman, Magnetic structures of TbMn_6Sn_6 and HoMn_6Sn_6 compounds from neutron diffraction study, *Journal of the Less Common Metals* **175**, 143 (1991).
 - [26] Y. Lee, R. Skomski, X. Wang, P. P. Orth, Y. Ren, B. Kang, A. K. Pathak, A. Kutepov, B. N. Harmon, R. J. McQueeney, I. I. Mazin, and L. Ke, Interplay between magnetism and band topology in the kagome magnets rmn_6sn_6 , *Phys. Rev. B* **108**, 045132 (2023).
 - [27] L. B. McCusker, R. B. Von Dreele, D. E. Cox, D. Louër, and P. Scardi, Rietveld refinement guidelines, *J. Appl. Cryst.* **32**, 36 (1999).
 - [28] J. Rodriguez-Carvajal, Recent advances in magnetic structure determination by neutron powder diffraction, *Physica B* **192**, 55 (1993).
 - [29] P. Giannozzi, O. Andreussi, T. Brumme, O. Bunau, M. B. Nardelli, M. Calandra, R. Car, C. Cavazzoni, D. Ceresoli, M. Cococcioni, and *et al.*, Advanced capabilities for materials modelling with QUANTUM ESPRESSO, *J. Phys.: Condens. Matter* **29**, 465901 (2017).
 - [30] A. A. Mostofi, J. R. Yates, G. Pizzi, Y.-S. Lee, I. Souza, D. Vanderbilt, and N. Marzari, An updated version of wannier90: A tool for obtaining maximally-localised wannier functions, *Computer Physics Communications* **185**, 2309 (2014).

- [31] D. Xiao, M.-C. Chang, and Q. Niu, Berry phase effects on electronic properties, *Rev. Mod. Phys.* **82**, 1959 (2010).
- [32] N. Nagaosa, J. Sinova, S. Onoda, A. H. MacDonald, and N. P. Ong, Anomalous hall effect, *Rev. Mod. Phys.* **82**, 1539 (2010).
- [33] X. Wang, D. Vanderbilt, J. R. Yates, and I. Souza, Fermi-surface calculation of the anomalous hall conductivity, *Phys. Rev. B* **76**, 195109 (2007).
- [34] X. Wang, J. R. Yates, I. Souza, and D. Vanderbilt, Ab initio calculation of the anomalous hall conductivity by wannier interpolation, *Phys. Rev. B* **74**, 195118 (2006).
- [35] Y. Yao, L. Kleinman, A. H. MacDonald, J. Sinova, T. Jungwirth, D.-s. Wang, E. Wang, and Q. Niu, First principles calculation of anomalous hall conductivity in ferromagnetic bcc fe, *Phys. Rev. Lett.* **92**, 037204 (2004).
- [36] Q. Wu, S. Zhang, H.-F. Song, M. Troyer, and A. A. Soluyanov, Wanniertools : An open-source software package for novel topological materials, *Computer Physics Communications* **224**, 405 (2018).
- [37] S. S. Tsirkin, High performance Wannier interpolation of Berry curvature and related quantities with Wannier-Berri code, *npj Computational Materials* **7**, 33 (2021).
- [38] G. Pizzi, V. Vitale, R. Arita, S. Blügel, F. Freimuth, G. Géranton, M. Gibertini, D. Gresch, C. Johnson, T. Koretsune, J. Ibañez-Azpiroz, H. Lee, J.-M. Lihm, D. Marchand, A. Marrazzo, Y. Mokrousov, J. I. Mustafa, Y. Nohara, Y. Nomura, L. Paulatto, S. Poncé, T. Ponweiser, J. Qiao, F. Thöle, S. S. Tsirkin, M. Wierzbowska, N. Marzari, D. Vanderbilt, I. Souza, A. A. Mostofi, and J. R. Yates, Wannier90 as a community code: new features and applications, *Journal of Physics: Condensed Matter* **32**, 165902 (2020).
- [39] K. Koepernik and H. Eschrig, Full-potential nonorthogonal local-orbital minimum-basis band-structure scheme, *Phys. Rev. B* **59**, 1743 (1999).
- [40] V. L. Grigoryan, J. Xiao, X. Wang, and K. Xia, Anomalous Hall effect scaling in ferromagnetic thin films, *Phys. Rev. B* **96**, 144426 (2017).
- [41] A. Crepieux and P. Bruno, Theory of the anomalous Hall effect from the Kubo formula and the Dirac equation, *Phys. Rev. B* **64**, 014416 (2001).
- [42] Y. Tian, L. Ye, and X. Jin, Proper scaling of the anomalous hall effect, *Phys. Rev. Lett.* **103**, 087206 (2009).
- [43] L. Ye, M. Kang, J. Liu, F. Von Cube, C. R. Wicker, T. Suzuki, C. Jozwiak, A. Bostwick, E. Rotenberg, D. C. Bell, L. Fu, R. Comin, and J. G. Checkelsky, Massive Dirac fermions in a ferromagnetic kagome metal, *Nature* **555**, 638 (2018).
- [44] H. Zhang, J. Koo, C. Xu, M. Sretenovic, B. Yan, and X. Ke, Exchange-biased topological transverse thermoelectric effects in a Kagome ferrimagnet, *Nature Communications* **13**, 1091 (2022).
- [45] P. E. Siegfried, H. Bhandari, M. P. Ghimire, X. Jia, F. Rodolakis, L. Mcchesney, M. Hashimoto, D. Lu, Y. Cao, R. M. Tutchton, P. Kyriazi, S. M. Birnbaum, J. Singleton, S. Chikara, S. Das, I. I. Mazin, and N. J. Ghimire, Microscopic origin of the large intrinsic anomalous Hall conductivity in the 3D kagome magnet, Unpublished.
- [46] S. A. Yang, H. Pan, Y. Yao, and Q. Niu, Scattering universality classes of side jump in the anomalous Hall effect, *Phys. Rev. B* **83**, 125122 (2011).
- [47] M. Kim, J. Mravlje, M. Ferrero, O. Parcollet, and A. Georges, Spin-Orbit Coupling and Electronic Correlations in Sr_2RuO_4 , *Phys. Rev. Lett.* **120**, 126401 (2018).

Supplementary Information

SUPPLEMENTARY NOTE 1: MAGNETIC ANISOTROPY ENERGY

We derive our expression for the magnetic anisotropy energy for the collinear arrangement of the moments on the Tb- and Mn-sublattices on the classical (Langevin) level. We first write the standard partition function for the external magnetic field H parallel to the z -axis assuming the anisotropy is a small correction to the Zeeman term:

$$\mathcal{Z} = e^{-\beta F} = \int_0^{2\pi} d\varphi \int_0^\pi e^{-(HM_z)\beta} \sin\theta \, d\theta \quad (\text{S1})$$

$$= 2\pi \int_0^\pi e^{\beta HM \cos\theta} \sin\theta \, d\theta, \quad (\text{S2})$$

$$= \frac{4\pi \sinh(\beta HM)}{\beta HM}, \quad (\text{S3})$$

where $\beta = k_B T$ with k_B being the Boltzmann constant, M is the total magnetization, and θ is the angle between M and H .

The expectation value for the total magnetic moment is:

$$m = \frac{1}{\mathcal{Z}} \int_0^{2\pi} d\varphi \int_0^\pi M \cos\theta \, e^{\beta HM \cos\theta} \sin\theta \, d\theta \quad (\text{S4})$$

$$= M \coth(\beta HM) - \frac{1}{\beta H} \quad (\text{S5})$$

By defining the hexagonal axis c to lie along field direction z , then the magnetic anisotropy energy can written as

$$\mathcal{H}_{anis} = K M_z^2 = K M^2 \cos^2 \theta \quad (\text{S6})$$

where K is the 2nd order anisotropy coefficient.

For the easy-axis, parallel to H , the expectation value is

$$E_{\parallel} = \frac{1}{\mathcal{Z}} \int_0^{2\pi} d\varphi \int_0^\pi K M^2 \cos^2 \theta \, e^{\beta HM \cos\theta} \sin\theta \, d\theta \quad (\text{S7})$$

$$= K M^2 - \frac{2K}{\beta H} m \quad (\text{S8})$$

For the easy axis perpendicular H , the expectation value is

$$E_{\perp} = \frac{1}{\mathcal{Z}} \int_0^{2\pi} \cos^2 \varphi d\varphi \int_0^\pi K M^2 \sin^2 \theta \, e^{\beta HM \cos\theta} \sin\theta \, d\theta \quad (\text{S9})$$

$$= \frac{K}{\beta H} m \quad (\text{S10})$$

$$(\text{S11})$$

The effective magnetic anisotropy energy is thus

$$MAE = E_{\parallel} - E_{\perp} = K M^2 - \frac{3K}{\beta H} m \quad (\text{S12})$$

To eliminate H , we solve the transcendental equation $m = M \coth(\beta HM) - 1/\beta H$ for H , by rewriting it as

$$\mu = \coth(h) - \frac{1}{h}, \quad (\text{S13})$$

where $\mu = m/M$ and $h = \beta HM$.

One finds solutions for $\mu \rightarrow 0$ and $\mu \rightarrow 1$ by interpolating between the two:

$$h = \mu(2 - \mu + \frac{1}{1 - \mu}) \Rightarrow H = \frac{m}{\beta M^2}(2 - \frac{m}{M} + \frac{M}{M - m}) \quad (\text{S14})$$

$$MAE = KM^2 - 3K \frac{M^2}{2 - \frac{m}{M} + \frac{M}{M - m}} = Km^2 \frac{M^2}{3M^2 - 3Mm + m^2} \quad (\text{S15})$$

Note that $MAE \rightarrow Km^2$ at $T = 0$, where $m = M$, and $MAE \rightarrow \frac{1}{3}KM^2$ near T_C , where $M \rightarrow 0$.

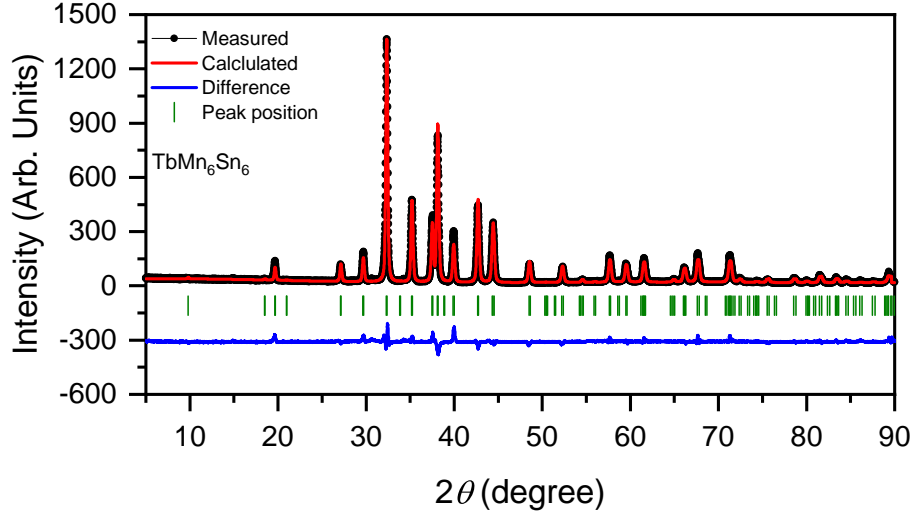


FIG. S1 : Rietveld refinement of the X-ray powder pattern of TbMn_6Sn_6 measured at room temperature.

TABLE S1 : Selected data from Rietveld refinement of powder X-ray diffraction collected on ground crystals of TbMn_6Sn_6 . Atomic coordinates are 0, 0, 0 for Tb; 0, $\frac{1}{2}$, z for Mn; 0, 0, z for Sn(1); $\frac{1}{3}$, $\frac{2}{3}$, $\frac{1}{2}$ for Sn(2); and $\frac{1}{3}$, $\frac{2}{3}$, 0 for Sn(3).

Space group	$P6/mmm$ (No. 191)
Unit cell parameters	$a = 5.5384(3) \text{ \AA}$
	$c = 9.0325(6) \text{ \AA}$
R_{WP}	14.6 %
R_B	8.61 %
R_F	7.43 %
Mn z coordinate	0.24803(31)
Sn(1) z coordinate	0.33325(26)

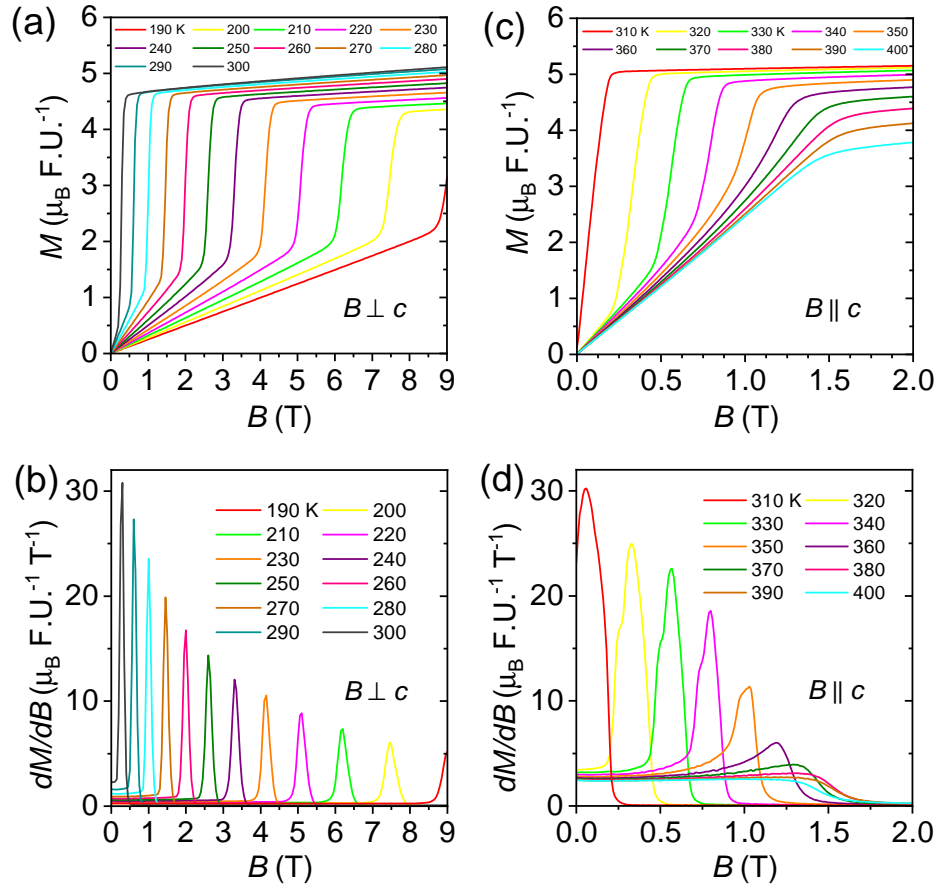


FIG. S2 : First Order Magnetization Process (FOMP) in TbMn₆Sn₆. (a) Magnetic field dependence of magnetization $M(B)$ with $B \perp c$ below the spin-reorientation transition temperature at zero-field T_{sr} . (b) Magnetic field dependence of derivative of magnetization $dM/dB(B)$ with $B \perp c$ below T_{sr} . (c) $M(B)$ with $B \parallel c$ above T_{sr} . (d) $dM/dB(B)$ with $B \parallel c$ above T_{sr} .

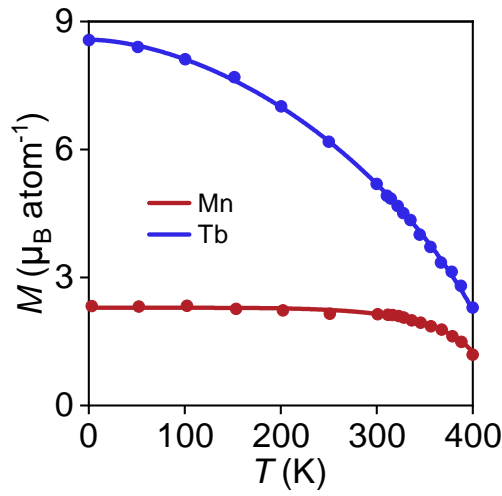


FIG. S3 : Fit of Brillouin curves (solid lines) to experimental data (points) for the temperature dependence on the magnetic moments on Mn and Tb obtained from a previous neutron powder diffraction study [25].

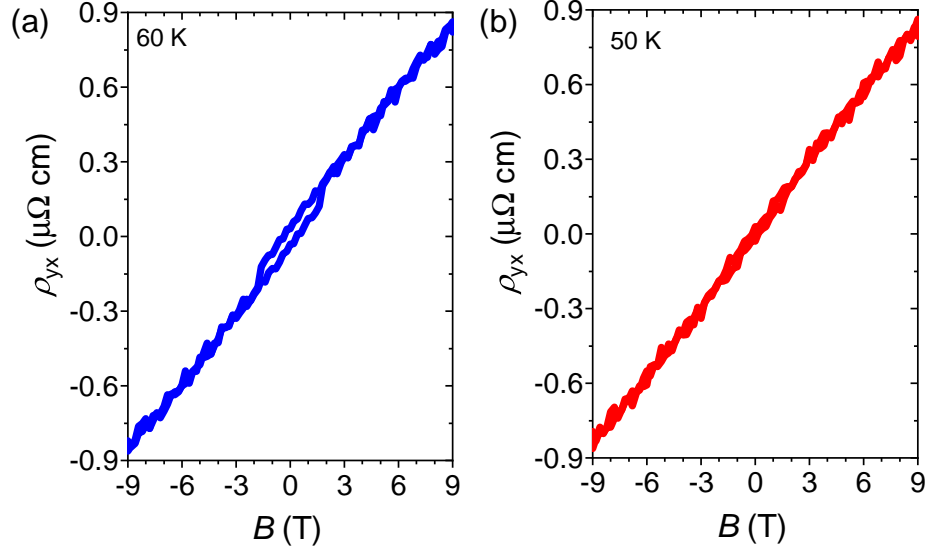


FIG. S4 : Hall resistivity as a function of magnetic field at a) 60 K and , b) 50 K. Note that there is a clear hysteresis in the Hall resistivity at 60 K, which allows to extract the anomalous Hall resistivity (ρ_{yx}^A) unambiguously. The hysteresis disappears (or is within the error bar of the resistivity measurement) at 50 K which does makes it difficult to get ρ_{yx}^A from these data at and below 50 K.

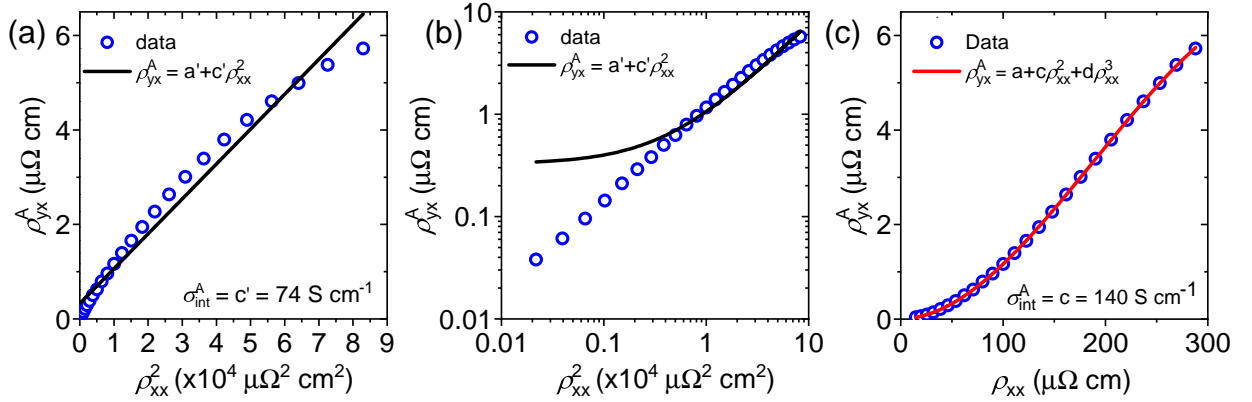


FIG. S5 : a) Anomalous Hall resistivity (ρ_{yx}^A) as a function of square of longitudinal resistivity (ρ_{xx}^2). Black line is a straight line fit to the data which shows that ρ_{yx}^A has a systematic deviation from the ρ_{xx}^2 dependence, which is more clearly seen in the log-log plot presented in Panel (b). Here, c' , the coefficient of ρ_{xx}^2 , gives the intrinsic anomalous Hall conductivity (ρ_{xy}^A), which is found to be 74 S cm^{-1} from this fit. c) ρ_{yx}^A vs. ρ_{xx} . The red line shows a fit to $a + c\rho_{xx}^2 + d\rho_{xx}^3$, which shows that the cubic term is necessary to describe the ρ_{xx} dependence of ρ_{yx}^A . ρ_{yx}^A obtained from this fitting is 140 S cm^{-1} .